APL Materials

# Self-assembly and properties of domain walls in $BiFeO_3$ layers grown via molecular-beam epitaxy

Cite as: APL Mater. **7**, 071101 (2019); https://doi.org/10.1063/1.5103244
Submitted: 25 April 2019 • Accepted: 06 June 2019 • Published Online: 02 July 2019

Antonio B. Mei, Yongjian Tang, Jürgen Schubert, et al.

# Self-assembly and properties of domain walls in $BiFeO_3$ layers grown via molecular-beam epitaxy

Cite as: APL Mater. 7, 071101 (2019); doi: 10.1063/1.5103244
Submitted: 25 April 2019 • Accepted: 6 June 2019 •
Published Online: 2 July 2019



Antonio B. Mei,[1,a] Yongjian Tang,[2] Jürgen Schubert,[3] Debdeep Jena,[1,4,5] Huili (Grace) Xing,[1,4,5] Daniel C. Ralph,[2,5] and Darrell G. Schlom[1,5]

## AFFILIATIONS

[1]Department of Materials Science and Engineering, Cornell University, Ithaca, New York 14853, USA
[2]Physics Department, Cornell University, Ithaca, New York 14853, USA
[3]Peter Grünberg Institute (PGI-9) and JARA-Fundamentals of Future Information Technology, Forschungszentrum Jülich GmbH, 52425 Jülich, Germany
[4]School of Electrical and Computer Engineering, Cornell University, Ithaca, New York 14853, USA
[5]Kavli Institute at Cornell for Nanoscale Science, Ithaca, New York 14853, USA

[a)]amei2@illinois.edu

## ABSTRACT

Bismuth ferrite layers, ~200-nm-thick, are deposited on $SrRuO_3$-coated $DyScO_3(110)_o$ substrates in a step-flow growth regime via adsorption-controlled molecular-beam epitaxy. Structural characterization shows the films to be phase pure with substrate-limited mosaicity (0.012° x-ray diffraction $\omega$-rocking curve widths). The film surfaces are atomically smooth (0.2 nm root-mean-square height fluctuations) and consist of 260-nm-wide $[1\bar{1}1]_o$-oriented terraces and unit-cell-tall (0.4 nm) step edges. The combination of electrostatic and symmetry boundary conditions promotes two monoclinically distorted $BiFeO_3$ ferroelectric variants, which self-assemble into a pattern with unprecedentedly coherent periodicity, consisting of 145 ± 2-nm-wide stripe domains separated by $[001]_o$-oriented 71° domain walls. The walls exhibit electrical rectification and enhanced conductivity.



## I. INTRODUCTION

The control of topological textures within the lattice, charge, and spin order parameters of multiferroic materials offers the possibility to realize emergent behaviors that transcend the functionality of any spatially uniform host material. Indeed, ferroelectric domain walls are already employed in various applications spanning nonlinear optics,[1,2] nanoelectronics,[3] and nonvolatile memories.[4,5]

Epitaxial layers of the room-temperature multiferroic $BiFeO_3$ are a well-established material platform for hosting domain walls with functional properties.[6] To date, the overwhelming majority of $BiFeO_3$ films are produced using far-from-equilibrium growth techniques incorporating ion irradiation during film growth, including magnetron sputter deposition[7] and pulsed-laser deposition.[8] When uncontrolled, ions spawn unintended defects impacting domain wall morphology and properties.[9,10] Molecular-beam epitaxy, in contrast, provides an alternative synthesis approach which employs thermalized molecular fluxes.[11] Near-equilibrium growth regimes free from the bombardment of energetic ions[12] are expected to engender subtler defect profiles,[13] desirable for the fabrication of nonlinear optical elements as well as for understanding leakage mechanisms in nonvolatile ferroelectric-based memories.

In this letter, we employ molecular-beam epitaxy[11,14] to grow commensurately strained $BiFeO_3/SrRuO_3/DyScO_3(110)_o$ epitaxial heterostructures (the *o* subscript designates orthorhombic indices in the nonstandard *Pbnm* setting) and demonstrate the self-assembly of

**TABLE I**. Conditions employed for the synthesis of the $BiFeO_3/SrRuO_3/DyScO_3(110)_o$ heterostructure described in this letter. The growths are carried out using molecular-beam epitaxy in an adsorption-controlled regime. $T_s$ are substrate temperatures, estimated using a thermocouple in the vicinity of, but not in direct contact with, the growth surface. $P$ are partial pressures during deposition of an oxidant comprised of approximately 20% $O_2$ and 80% $O_3$, produced by controllably degassing ozone-infused silica beads. $J_{A=Bi,Sr}$ and $J_{B=Fe,Ru}$ are molecular fluxes, measured using a calibrated quartz-crystal microbalance. $T_{A=Bi,Sr}$ and $T_{B=Fe}$ are effusion cell temperatures (Ru is supplied from an electron-beam source). $R$ are film growth rates.

| | $T_s$ | $P$ | $J_A$ | $J_B$ | $T_A$ | $T_B$ | $R$ |
|---|---|---|---|---|---|---|---|
| | °C | $10^{-6}$ Torr | $10^{13}$ cm$^2$ s | | °C | | nm/min |
| $BiFeO_3$ | 650 | 10.0 | 38.0 | 2.4 | 650 | 1250 | 1.10 |
| $SrRuO_3$ | 780 | 1.0 | 3.1 | 6.7 | 500 | ... | 1.15 |

ferroelectric $BiFeO_3$ domain walls with unprecedentedly long-range order. The walls exhibit the combination of enhanced conductivity and electrical rectification. We anticipate that the results discussed here may prove useful for improving the fabrication of nonlinear optical and nanoelectronic devices.

## II. RESULTS

### A. Film growth

$BiFeO_3/SrRuO_3/DyScO_3(110)_o$ heterostructures are grown without breaking vacuum in a Veeco GEN10 molecular-beam epitaxy system with a chamber base pressure of $1 \times 10^{-8}$ Torr using deposition conditions summarized in Table I. For $SrRuO_3$ growths, ruthenium is supplied in abundance with a ruthenium-to-strontium flux ratio of $J_{Ru}/J_{Sr} > 2$. At a growth temperature of 780°, the excess ruthenium oxidizes forming volatile $RuO_x$ species which continuously desorb from the growth surface resulting in single-phase $SrRuO_3$ layers.[15] $BiFeO_3$ is grown in an oxidant comprised chiefly of ozone (and 20% oxygen). This approach, which represents an evolution of increasing oxidation environments,[14,16–20] helps to suppress the formation of oxygen vacancies, responsible for engendering mobile electrons[21] and ensures the oxidation of bismuth.[14] Additionally, high bismuth-to-iron flux ratios ($J_{Bi}/J_{Fe} \sim 16$) are employed to compensate the loss of volatile $BiO_x$ species at the high homologous growth temperature utilized (Ts ~ 650); the desorption of bismuth oxides during $BiFeO_3$ deposition is analogous to that of ruthenium oxides during $SrRuO_3$ growth. Although multiple films were grown and all findings presented here (and in the supplementary material) are obtained from a single film, for which Rutherford back scattering spectrometry results yield a film bismuth-to-iron molar ratio equal to 0.98 ± 0.07. The deposition of stoichiometric layers, containing equal concentrations of bismuth and iron, combined with long diffusion lengths for surface adatoms promote films with long-ranged crystallographic and ferroic order.

### B. Film structural perfection

The structural perfection of $BiFeO_3$ layers deposited on $SrRuO_3$-coated $DyScO_3(110)$ substrates is established using the combination of x-ray diffraction (XRD), atomic force microscopy (AFM), and scanning transmission electron microscopy (STEM). An XRD $\theta$–$2\theta$ scan (see Fig. S1 of the supplementary material) collected between $10 \le 2\theta \le 110°$ using Cu $K_{\alpha 1}$ radiation (wavelength $\lambda$ = 0.154 06 nm) exhibits only $00l_p$ film and $hh0_o$ substrate reflections (the $p$ subscript refers to pseudocubic indices); the absence of additional reflections evince a phase-pure single crystalline film.

Figure 1(a) highlights diffracted intensity oscillations[22] near $DyScO_3$ $110_o$, which result from the interference of x-rays reflected at $BiFeO_3$ and $SrRuO_3$ interfaces. Measured intensities are accurately reproduced by simulations[23,24] based on a heterostructure with atomically sharp interfaces, pseudocubic out-of-plane lattice parameters $a_\perp$ of 0.3991 ($BiFeO_3$), 0.3942 ($SrRuO_3$), and 0.3939 nm ($DyScO_3$), film thicknesses of 217 ($BiFeO_3$) and 23 nm ($SrRuO_3$), and a thickness-limited film out-of-plane mosaic coherence. The in-plane mosaic coherence length, ~2 $\mu$m, is determined[25] from the full-width-at-half-maximum (FWMH) value of the $BiFeO_3$

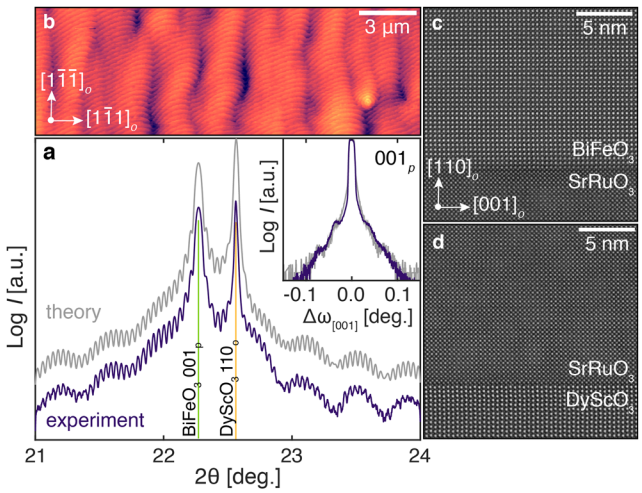


**FIG. 1**. Structural perfection of a commensurate $BiFeO_3/SrRuO_3$ heterostructure grown on $DyScO_3(110)_o$. (a) XRD $\theta$–$2\theta$ intensities (purple) agree with simulation results (gray) based on an ideal heterostructure. Overlapping $BiFeO_3$ $001_p$ (purple) and $DyScO_3$ $110_p$ (gray) $\omega$-rocking curve scans (inset) attest to a high substrate-limited film structural perfection; full-width-at-half-maxima values for film and substrate peaks are both 0.012° (43 arc sec), corresponding to in-plane mosaic coherence lengths of ~2 $\mu$m. (b) Surface height modulations, as measured via AFM, establish an atomically smooth film surface with unit-cell-tall (0.4 nm) step edges. Lattice-resolution STEM images collected along the $[1\bar{1}0]_o$ zone axis demonstrate commensurate and abrupt (c) $BiFeO_3/SrRuO_3$ and (d) $SrRuO_3/DyScO_3$ interfaces. The coordinates on (b) and (c) refer to the axes of the $DyScO_3$ substrate.

$001_p$ reflection (0.012° = 43 arcsec), measured along $[001]_o$ using $\omega$-rocking curve scans [Fig. 1(a), insert]. The FWHM value measured for the $BiFeO_3$ reflection is the same as that for the underlying $DyScO_3$ and demonstrates that the film structural perfection is limited by the intrinsic mosaicity of the substrate.

From lattice-resolution STEM images obtained along the $[1\bar{1}0]_o$ zone axis near $BiFeO_3/SrRuO_3$ [Fig. 1(c)] and $SrRuO_3/DyScO_3$ [Fig. 1(d)], we find atomically abrupt heterostructure interfaces with commensurate *pseudo* cube-on-cube crystallographic stacking: $BiFeO_3(001)[100]_p \parallel SrRuO_3(001)[100]_p \parallel DyScO_3(110)[001]_o$.

AFM height images, including Fig. 1(b), evince smooth surfaces (0.2 nm root-mean-square height fluctuations) over macroscopic distances ($\gtrsim$20 $\mu$m) with motifs including unit-cell-tall (0.4 nm) step-edges oriented parallel to $BiFeO_3$ $[110]_p$ and $DyScO_3$ $[1\bar{1}1]_o$, 260-nm-wide $[1\bar{1}1]_o$-oriented terraces (0.09° miscut), and shallow islands (areal density $\lesssim 10^6$ cm$^{-2}$). The latter, through analyses of *in situ* reflection high-energy electron diffraction (RHEED) patterns (see Fig. S2 of the supplementary material), are determined to form during the layer-by-layer growth of $SrRuO_3$.

### C. Symmetry breaking and wall self-assembly

To investigate the breaking of cubic symmetries and the emergence of topological features within $BiFeO_3$, we perform XRD reciprocal space maps (RSM), lateral (LPFM), and vertical (VPFM) piezoforce microscopy (PFM), and bright-field transmission electron microscopy (BF-TEM).[53] RSM analyses carried out about film peaks reveal that the $BiFeO_3$ $103_p$ and $113_p$ family of reflections are split into doublets and triplets [Fig. 2(a)], consistent with monoclinically distorted pseudocubic unit cells that have been sheared along $\langle 110 \rangle_p$.[26] The descent in symmetry from the cubic perovskite to the monoclinic structure is accompanied by polar $\langle 111 \rangle_p$ cation displacements and antiferrodistortive $a^-a^-a^-$ antiphase $FeO_6$ octahedral rotations.[27] The symmetry-breaking process engenders four structural and eight ferroelectric variants, represented by $r_\psi^\pm$, in which the subscript $\psi$ identifies the azimuthal orientation of the in-plane polarization component and the superscript ± selects the out-of-plane component. Analyzing the intensity variation of the $103_p$ and $113_p$ family of peaks [see Fig. 2(a)] reveals that the $BiFeO_3$ layer consists primarily of two structural variants, $r_{+45°}$ and $r_{-45°}$, which develop due to the orthorhombic symmetry of the $DyScO_3$ substrate.[28] The volume fraction occupied by the dominant vs secondary structural variants is estimated from ratios of RSM peak integrals to be $\gtrsim$0.99. These findings are corroborated by PFM analyses [e.g., Fig. 2(b)], which exhibit a two-level contrast.

To determine the out-of-plane polarization orientation, ferroelectric domains are locally poled by applying ±15 V tip biases to a conductive probe while rastering it across the sample surface. Plan-view VPFM images (see Fig. S3 of the supplementary material) demonstrate that in regions where the tip is negatively biased, changes in contrast are observed due to the polarization being poled toward the tip. That the out-of-plane polarization component of as-deposited layers is homogeneously aligned toward the substrate is consistent with the A-site termination of our $SrRuO_3$ electrode, which encourages the $BiFeO_3$ polarization to orient in such a way that a depolarization field develops to counteract a built-in field associated with the valence states of each perovskite layer.[29]

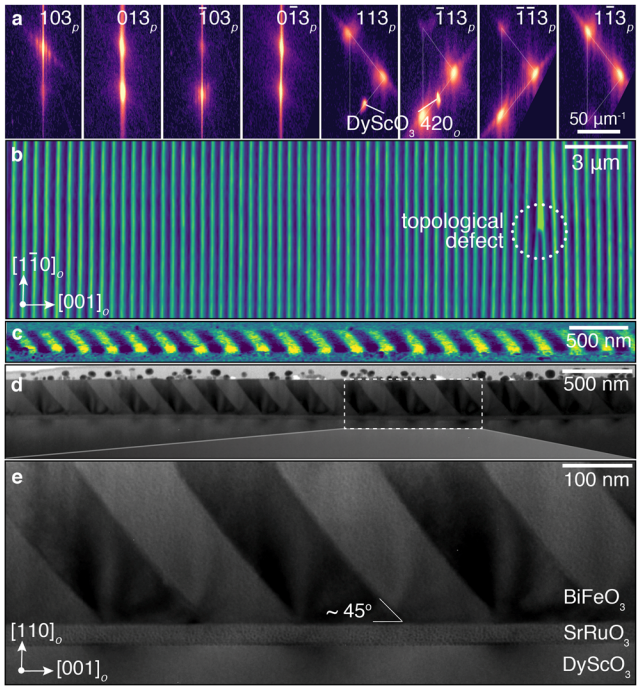


**FIG. 2.** Self-assembled walls in monoclinic $BiFeO_3$ following spontaneous cubic-symmetry breaking. (a) RSMs show splitting of the $103_p$ and $113_p$ family of peaks into doublets and triplets following a monoclinic distortion which develops through the combination of cubic symmetry breaking and commensurate epitaxial strain. (b) Plan-view LPFM and (c) cross-sectional VPFM images reveal a one-dimensional array of self-assembled domain walls with unprecedented long-range perfection, in agreement with cross-sectional BF-TEM findings, (d) and (e). The coordinates on (b) and (e) refer to the axes of the $DyScO_3$ substrate.

Between regions of uniform polarization are domain walls, two-dimensional topological field excitations that emerge when the potential energy describing the order parameter consists of deep valleys and disconnected ground states.[30] Plan-view LPFM [Fig. 2(b)], cross-sectional VPFM [Fig. 2(c)], and cross-sectional BF-TEM micrographs [Figs. 2(d) and 2(e)] show that the domain walls in our as-grown $BiFeO_3$ layers self-assemble into a periodic quasi-one-dimensional stripe array along $DyScO_3$ $[001]_o$ with inter-wall separations measuring 145 ± 2 nm. The walls are found to be inclined ~45° relative to the surface normal [Figs. 2(c)–2(e)], in agreement with geometric considerations for 71° walls (the wall type is labeled based on the angle formed between polarization vectors in adjacent domains) residing on $\{110\}_p$ planes.[31,32] In previous work, it was shown that the inclination angle and the wall type can be controlled by changing boundary conditions[28] and film thicknesses;[33] similarly, the wall orientation can be tuned through the application of biaxial in-plane strain[34,35] from $\langle 100 \rangle_p$ for $1.5\% \lesssim m \lesssim 0.3\%$ to $\langle 110 \rangle_p$ for $m \approx 3.6\%$, in which $m$ is the lattice mismatch between the $BiFeO_3$ film and the underlying substrate.[35–39]

The stripe domains are occasionally seen to terminate within the film, giving rise to one-dimensional topological defects analogous to dislocations [the dotted circle in Fig. 2(b)]. Despite the one

defect that we observe in a $\gtrsim 20\ \mu$m field of view, the structural perfection of the pattern realized here represents the most well-ordered self-assembled array of ferroelastic domain walls produced to date.[33,35,36,40–46]

### D. Electrical properties of walls

The electrical properties of the $BiFeO_3/SrRuO_3/DyScO_3(110)_o$ heterostructure are investigated using conductive AFM (c-AFM), by grounding the bottom $SrRuO_3$ electrode and rastering a biased tip in contact with the sample surface while recording through-layer currents. Typical results, shown in Figs. 3(a)–3(d), establish that no current flows for biases $V_b \leq 1$ V (detectable current limit ~1pA). In the $2 \leq V_b \leq 3$ V regime, the current is preferentially emitted at domain walls, where the conductivity is two to ten times higher than at domains [see the current histogram in Fig. 3(e)]. At a bias of $V_b = 4$ V, the corresponding electric field across the film, 180 kV/cm, exceeds the coercive field of bismuth ferrite, ~170 kV/cm.[44] As a consequence, c-AFM images acquired under these conditions, including Fig. 3(d), contain contributions from both resistive and displacement currents as a result of domains being locally poled.

Macroscopic current-voltage $I(V)$ measurements, obtained by integrating the c-AFM measurements over a $5 \times 5\ \mu m^2$ area, Fig. 3(f), highlight the existence of rectifying behavior, agreeing with previous reports.[9,10] The enhanced conduction at 71° domain walls can be understood to result from a combination of effects which include a reduction in the $BiFeO_3$ conduction band energy and an accumulation of intrinsic defects,[10,47] including double-donor[21] oxygen vacancy states, near the walls. The asymmetric response, which produces the rectifying behavior, is attributed to the combination of dissimilar emission barrier heights across the film/electrode and film/tip interface as well as to the presence of an out-of-plane film polarization which breaks up/down symmetry.[48] For the measurement conditions employed, Joule heating is estimated[49,51,52] to cause a temperature rise of only ~0.03 K; for reference, electric fields are expected to trigger breakdown in perovskite oxides only above ~2000 kV/cm,[50] five to ten times larger than the largest values applied here.

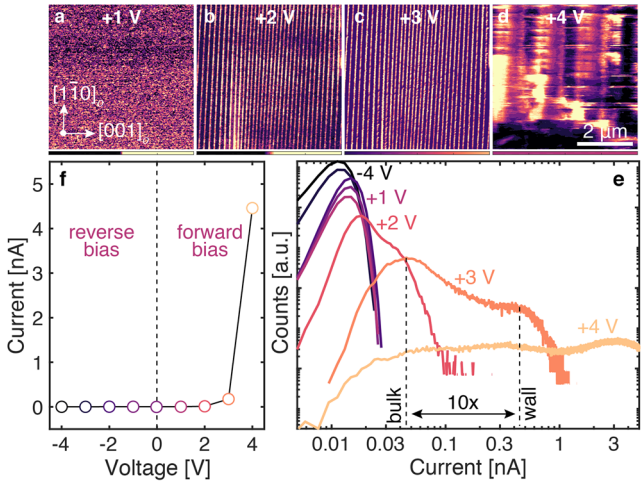


**FIG. 3.** Electrical conduction at 71° domain walls in a $BiFeO_3$ layer deposited on a $SrRuO_3$-coated $DyScO_3(110)_o$ substrate. c-AFM maps show current flow over a $5 \times 5\ \mu m^2$ area under increasing tip biases of (a) +1, (b) +2, (c) +3, and (d) +4 V. (e) Current histograms reveal that at 3 V bias, conduction is ten times higher at walls than at domains. (f) $I(V)$ measurements, obtained by averaging the current collected over the area corresponding to panels (a)–(d), exhibit diode-like rectifying behavior. The color range in (a)–(d) spans ±0.2 nA. The coordinates in (a) refer to the axes of the $DyScO_3$ substrate.

## III. CONCLUSIONS

The ability to produce ordered walls with well-ordered periodicity, as demonstrated here, could have immediate technological implications. For example, domain walls are already lithographically introduced into commercial nonlinear crystals to help satisfy momentum conservation in three-photon interactions. These processes, which include sum frequency generation and parametric down conversion, are essential for up-converting laser frequencies as well as entangling photons for quantum computation. Being able to produce arrays of walls which self-assemble into high-fidelity patterns could provide a bottom-up alternative for the fabrication of such nonlinear optical elements. Additionally, the perfection of the patterns realized here reflects an intrinsically low concentration of defects. The realization of films with low defect density are necessary to produce energy efficient memories with ferroic orders that can be easily switched at low coercive fields without wall pinning. Finally, the 71° domain walls are shown to simultaneously exhibit enhanced conductivity and electrical rectification—attributes which are desirable for emerging nanoelectronic applications, including domain wall memories.[4]

## SUPPLEMENTARY MATERIAL

Additional film characterization, including XRD $\theta$–$2\theta$, RHEED, and VPFM, is provided in the supplementary material.

## ACKNOWLEDGMENTS

This work was supported in part by the Semiconductor Research Corporation (SRC) as nCORE task No. 2758.003 and NSF under the E2CDA (ECCS 1740286) and MRI (Grant No. 1338010) programs. This work made use of the Cornell Center for Materials Research (CCMR) Shared Facilities, which are supported through the NSF MRSEC program (Grant No. DMR-1719875). Substrate preparation was performed in part at the Cornell NanoScale Facility, a member of the National Nanotechnology Coordinated Infrastructure (NNCI), which is supported by the NSF (Grant No. ECCS-1542081).

## REFERENCES

[1] J. A. Armstrong, N. Bloembergen, J. Ducuing, and P. S. Pershan, Phys. Rev. **127**, 1918 (1962).
[2] L. E. Myers, R. C. Eckardt, M. M. Fejer, and R. L. Byer, in *Photonics West '95*, edited by G. J. Quarles, L. Esterowitz, and L. K. Cheng (SPIE, 1995), pp. 154–162.
[3] G. Catalan, J. Seidel, R. Ramesh, and J. F. Scott, Rev. Mod. Phys. **84**, 119 (2012).
[4] P. Sharma, Q. Zhang, D. Sando, C. H. Lei, Y. Liu, J. Li, V. Nagarajan, and J. Seidel, Sci. Adv. **3**, e1700512 (2017).

[5]J. Ma, J. Ma, Q. Zhang, R. Peng, J. Wang, C. Liu, M. Wang, N. Li, M. Chen, X. Cheng, P. Gao, L. Gu, L.-Q. Chen, P. Yu, J. Zhang, and C.-W. Nan, Nat. Nanotechnol. **13**, 947 (2018).
[6]G. A. Smolenskiĭ and I. E. Chupis, Usp. Fizicheskih Nauk **137**, 415 (1982).
[7]C. M. Folkman, S. H. Baek, H. W. Jang, C. B. Eom, C. T. Nelson, X. Q. Pan, Y. L. Li, L. Q. Chen, A. Kumar, V. Gopalan, and S. K. Streiffer, Appl. Phys. Lett. **94**, 251911 (2009).
[8]J. Wang, J. B. Neaton, H. Zheng, V. Nagarajan, S. B. Ogale, B. Liu, D. Viehland, V. Vaithyanathan, D. G. Schlom, U. V. Waghmare, N. A. Spaldin, K. M. Rabe, M. Wuttig, and R. Ramesh, Science **299**, 1719 (2003).
[9]J. Seidel, P. Maksymovych, Y. Batra, A. Katan, S. Y. Yang, Q. He, A. P. Baddorf, S. V. Kalinin, C. H. Yang, J. C. Yang, Y. H. Chu, E. K. H. Salje, H. Wormeester, M. Salmeron, and R. Ramesh, Phys. Rev. Lett. **105**, 197603 (2010).
[10]T. Rojac, A. Bencan, G. Drazic, N. Sakamoto, H. Ursic, B. Jancar, G. Tavcar, M. Makarovic, J. Walker, B. Malic, and D. Damjanovic, Nat. Mater. **16**, 322 (2017).
[11]D. G. Schlom, APL Mater. **3**, 062403 (2015).
[12]I. Petrov, P. B. Barna, L. Hultman, and J. E. Greene, J. Vac. Sci. Technol., A **21**, S117 (2003).
[13]D. G. Schlom, L.-Q. Chen, X. Pan, A. Schmehl, and M. A. Zurbuchen, J. Am. Ceram. Soc. **91**, 2429 (2008).
[14]E. H. Smith, J. F. Ihlefeld, C. A. Heikes, H. Paik, Y. Nie, C. Adamo, T. Heeg, Z.-K. Liu, and D. G. Schlom, Phys. Rev. Mater. **1**, 023403 (2017).
[15]H. P. Nair, Y. Liu, J. P. Ruf, N. J. Schreiber, S.-L. Shang, D. J. Baek, B. H. Goodge, L. F. Kourkoutis, Z.-K. Liu, K. M. Shen, and D. G. Schlom, APL Mater. **6**, 046101 (2018).
[16]J. Kabelac, S. Ghosh, P. Dobal, and R. Katiyar, J. Vac. Sci. Technol., B: Microelectron. Nanometer Struct. **25**, 1049 (2007).
[17]J. F. Ihlefeld, A. Kumar, V. Gopalan, D. G. Schlom, Y. B. Chen, X. Q. Pan, T. Heeg, J. Schubert, X. Ke, P. Schiffer, J. Orenstein, L. W. Martin, Y. H. Chu, and R. Ramesh, Appl. Phys. Lett. **91**, 071922 (2007).
[18]J. F. Ihlefeld, N. J. Podraza, Z. K. Liu, R. C. Rai, X. Xu, T. Heeg, Y. B. Chen, J. Li, R. W. Collins, J. L. Musfeldt, X. Q. Pan, J. Schubert, R. Ramesh, and D. G. Schlom, Appl. Phys. Lett. **92**, 142908 (2008).
[19]J. F. Ihlefeld, W. Tian, Z.-K. Liu, W. A. Doolittle, M. Bernhagen, P. Reiche, R. Uecker, R. Ramesh, and D. G. Schlom, IEEE Trans. Sonics Ultrason., Ferroelectr., Freq. Control **56**, 1528 (2009).
[20]J. A. Mundy, C. A. Heikes, B. F. Grosso, D. F. Segedin, Z. Wang, B. H. Goodge, Q. N. Meier, C. T. Nelson, B. Prasad, L. F. Kourkoutis, W. D. Ratcliff, N. A. Spaldin, R. Ramesh, and D. G. Schlom, e-print arXiv:1812.09615 (2018), p. 1.
[21]S. J. Clark and J. Robertson, Appl. Phys. Lett. **94**, 022902 (2009).
[22]M. Laue, Ann. Phys. **346**, 989 (1913).
[23]S. Takagi, Acta Crystallogr. **15**, 1311 (1962).
[24]W. J. Bartels, J. Hornstra, and D. J. W. Lobeek, Acta Crystallogr., Sect. A: Found. Crystallogr. **42**, 539 (1986).
[25]A. B. Mei, R. B. Wilson, D. Li, D. G. Cahill, A. Rockett, J. Birch, L. Hultman, J. E. Greene, and I. Petrov, J. Appl. Phys. **115**, 214908 (2014).
[26]The monoclinic deformation changes the lengths of the ideal cubic perovskite diagonals. When projected on $100_p$, the resulting unit cells have the shape of parallelograms with inequivalent major and minor diagonals. The shortening of the minor diagonal in real space moves the corresponding diffraction peak farther from the origin in diffraction space. Conversely, the lengthening of the major diagonal causes the Bragg peak to shift closer to the origin. The fact that the peaks split rather than shift can be understood to arise from a superposition of both these effects in the presence of multiple structural variants. On $110_p$ diffraction planes, in addition to the two parallelograms, the unit cell also projects as a square, giving rise to apical reflections.
[27]A. M. Glazer, Acta Crystallogr., Sect. B: Struct. Crystallogr. Cryst. Chem. **28**, 3384 (1972).
[28]Z. H. Chen, A. R. Damodaran, R. Xu, S. Lee, and L. W. Martin, Appl. Phys. Lett. **104**, 182908 (2014).
[29]P. Yu, W. Luo, D. Yi, J. X. Zhang, M. D. Rossell, C. H. Yang, L. You, G. Singh-Bhalla, S. Y. Yang, Q. He, Q. M. Ramasse, R. Erni, L. W. Martin, Y. H. Chu, S. T. Pantelides, S. J. Pennycook, and R. Ramesh, Proc. Natl. Acad. Sci. U. S. A. **109**, 9710 (2012).
[30]T. W. B. Kibble, J. Phys. A: Math. Gen. **9**, 1387 (1976).
[31]S. K. Streiffer, C. B. Parker, A. E. Romanov, M. J. Lefevre, L. Zhao, J. S. Speck, W. Pompe, C. M. Foster, and G. R. Bai, J. Appl. Phys. **83**, 2742 (1998).
[32]A. Lubk, S. Gemming, and N. A. Spaldin, Phys. Rev. B **80**, 104110 (2009).
[33]Y.-H. Chu, Q. He, C.-H. Yang, P. Yu, L. W. Martin, P. Shafer, and R. Ramesh, Nano Lett. **9**, 1726 (2009).
[34]H. M. Christen, J. H. Nam, H. S. Kim, A. J. Hatt, and N. A. Spaldin, Phys. Rev. B **83**, 144107 (2011).
[35]Z. Chen, Z. Luo, C. Huang, Y. Qi, P. Yang, L. You, C. Hu, T. Wu, J. Wang, C. Gao, T. Sritharan, and L. Chen, Adv. Funct. Mater. **21**, 133 (2010).
[36]Y. H. Chu, Q. Zhan, L. W. Martin, M. P. Cruz, P. L. Yang, G. W. Pabst, F. Zavaliche, S. Y. Yang, J. X. Zhang, L. Q. Chen, D. G. Schlom, I. N. Lin, T. B. Wu, and R. Ramesh, Adv. Mater. **18**, 2307 (2006).
[37]N. Balke, S. Choudhury, S. Jesse, M. Huijben, Y. H. Chu, A. P. Baddorf, L. Q. Chen, R. Ramesh, and S. V. Kalinin, Nat. Nanotechnol. **4**, 868 (2009).
[38]Z. Luo, Z. Chen, Y. Yang, H.-J. Liu, C. Huang, H. Huang, H. Wang, M.-M. Yang, C. Hu, G. Pan, W. Wen, X. Li, Q. He, T. Sritharan, Y.-H. Chu, L. Chen, and C. Gao, Phys. Rev. B **88**, 064103 (2013).
[39]Z. Chen, J. Liu, Y. Qi, D. Chen, S.-L. Hsu, A. R. Damodaran, X. He, A. T. N'Diaye, A. Rockett, and L. W. Martin, Nano Lett. **15**, 6506 (2015).
[40]Y. H. Chu, T. Zhao, M. P. Cruz, Q. Zhan, P. L. Yang, L. W. Martin, M. Huijben, C. H. Yang, F. Zavaliche, H. Zheng, and R. Ramesh, Appl. Phys. Lett. **90**, 252906 (2007).
[41]Y. H. Chu, M. P. Cruz, C. H. Yang, L. W. Martin, P. L. Yang, J. X. Zhang, K. Lee, P. Yu, L. Q. Chen, and R. Ramesh, Adv. Mater. **19**, 2662 (2007).
[42]R. K. Vasudevan, Y.-C. Chen, H.-H. Tai, N. Balke, P. Wu, S. Bhattacharya, L. Q. Chen, Y.-H. Chu, I.-N. Lin, S. V. Kalinin, and V. Nagarajan, ACS Nano **5**, 879 (2011).
[43]A. R. Damodaran, S. Lee, J. Karthik, S. MacLaren, and L. W. Martin, Phys. Rev. B **85**, 024113 (2012).
[44]L. R. Dedon, S. Saremi, Z. Chen, A. R. Damodaran, B. A. Apgar, R. Gao, and L. W. Martin, Chem. Mater. **28**, 5952 (2016).
[45]Y. Sharma, R. Agarwal, C. Phatak, B. Kim, S. Jeon, R. S. Katiyar, and S. Hong, Sci. Rep. **7**, 4857 (2017).
[46]Y. Yun, N. Ramakrishnegowda, D.-S. Park, and A. Bhatnagar, Appl. Phys. Lett. **113**, 042901 (2018).
[47]S. Farokhipoor and B. Noheda, Phys. Rev. Lett. **107**, 127601 (2011).
[48]E. Y. Tsymbal and H. Kohlstedt, Science **313**, 181 (2006).
[49]The temperature rise caused by Joule heating is estimated[52] to be $\Delta T = Q/(t\kappa) \approx 0.03$ K, from the dissipated power $Q = 3$ nA $\times$ 4 V $\approx 1 \times 10^{-8}$ W, the bismuth ferrite film thickness $t \approx 200$ nm, and the $DyScO_3$ thermal conductivity $\kappa \approx 2$ $Wm^{-1}$ $K^{-1}$.[53]
[50]T. M. Correia, M. McMillen, M. K. Rokosz, P. M. Weaver, J. M. Gregg, G. Viola, and M. G. Cain, J. Am. Ceram. Soc. **96**, 2699 (2013).
[51]Y. Kim, A. Kumar, A. Tselev, I. I. Kravchenko, H. Han, I. Vrejoiu, W. Lee, D. Hesse, M. Alexe, S. V. Kalinin, and S. Jesse, ACS Nano **5**, 9104 (2011).
[52]J. Hidde, C. Guguschev, S. Ganschow, and D. Klimm, J. Alloys Compd. **738**, 415 (2018).
[53]Cross-sectional VPFM samples are prepared using a slicing and polishing procedure similar to that employed in making lamellas for cross-sectional TEM.

# Supplementary Material

FIG. S1. XRD θ-2θ scan between 10 to 110° collected from a $BiFeO_3/SrRuO_3/DyScO_3$ heterostructure grown via adsorption-controlled ozone molecular-beam epitaxy.

Figure S1 is a θ-2θ scan between 10 to 110° collected from a $BiFeO_3/SrRuO_3/DyScO_3$ heterostructure grown via adsorption-controlled ozone molecular-beam epitaxy. The peaks observed correspond to the $00l_p$ family of film and substrate reflections.

FIG. S2. RHEED patterns collected in situ following the deposition of (a) $SrRuO_3$ and (b) and (c) $BiFeO_3$. (a) and (b) are obtained along $[100]_p$ azimuth; (c) is acquired along $[110]_p$. The arcs demarcate regions where the specular condition is satisfied, i.e. where the incident and scattered electron beams form the same angle with the sample surface.

Figures S2(a) and S2(b) are RHEED patterns collected in situ along the $[100]_p$ azimuth following the growth of $SrRuO_3$ and $BiFeO_3$ layers, respectively. The streaked reflections in Fig. S2(a) are consistent with the layer-by-layer growth of $SrRuO_3$ and results from the formation of shallow islands on atomic terraces. The spots in Fig. S2(b) and S2(c) indicate that the growth of $BiFeO_3$ proceeds in a step-flow mode, promoting wide terraces.

FIG. S3. (a) VPFM and (b) AFM height image of a pattern generated by modulating the probe bias by ±15 V as a tip was rastered across the sample surface. The blue and green regions in (a) correspond to $BiFeO_3$ out-of-plane ferroelectric polarizations components which point towards and away from the $SrRuO_3$ bottom electrode. The coordinates on (a) and (b) refer to the axes of the $DyScO_3$ substrate.

Figure S3(a) is a plan-view VPFM image of a ferroelectric domain pattern generated by modulating the bias on a probe as it was rastered across the sample surface; Figure S3(b) is the corresponding AFM contact-mode height image showing the changes associated with the ferroelastic domain structure. These results demonstrate our ability to control the ferroelectric and ferroelastic order parameters of our $BiFeO_3/SrRuO_3/DyScO_3(110)_o$ heterostructures. Note that the region imaged in Figs. S3(a) and S3(b) includes the region shown in Fig. 1(b).